HHS Public Access

Author manuscript

Phys Med Biol. Author manuscript; available in PMC 2018 June 21.

Published in final edited form as:

Phys Med Biol. 2017 June 21; 62(12): 4777–4797. doi:10.1088/1361-6560/aa6a97.

Task-driven optimization of CT tube current modulation and regularization in model-based iterative reconstruction

Grace J. Gang, **Jeffrey H. Siewerdsen**, and **J. Webster Stayman**

Department of Biomedical Engineering, Johns Hopkins University, Baltimore, MD 21205, USA

Abstract

Tube current modulation (TCM) is routinely adopted on diagnostic CT scanners for dose reduction. Conventional TCM strategies are generally designed for filtered-backprojection (FBP) reconstruction to satisfy simple image quality requirements based on noise. This work investigates TCM designs for model-based iterative reconstruction (MBIR) to achieve optimal imaging performance as determined by a task-based image quality metric. Additionally, regularization is an important aspect of MBIR that is jointly optimized with TCM, and includes both the regularization strength that controls overall smoothness as well as directional weights that permits control of the isotropy/anisotropy of the local noise and resolution properties. Initial investigations focus on a known imaging task at a single location in the image volume. The framework adopts Fourier and analytical approximations for fast estimation of the local noise power spectrum (NPS) and modulation transfer function (MTF) - each carrying dependencies on TCM and regularization. For the single location optimization, the local detectability index (d') of the specific task was directly adopted as the objective function. A covariance matrix adaptation evolution strategy (CMA-ES) algorithm was employed to identify the optimal combination of imaging parameters. Evaluations of both conventional and task-driven approaches were performed in an abdomen phantom for a mid-frequency discrimination task in the kidney. Among the conventional strategies, the TCM pattern optimal for FBP using a minimum variance criterion yielded worse task-based performance compared to an unmodulated strategy when applied to MBIR. Moreover, task-driven TCM designs for MBIR were found to have the opposite behavior from conventional designs for FBP, with greater fluence assigned to the less attenuating views of the abdomen and less fluence to the more attenuating lateral views. Such TCM patterns exaggerate the intrinsic anisotropy of the MTF and NPS as a result of the data weighting in MBIR. Directional penalty design was found to reinforce the same trend. The task-driven approaches outperform conventional approaches, with the maximum improvement in d' of 13% given by the joint optimization of TCM and regularization. This work demonstrates that the TCM optimal for MBIR is distinct from conventional strategies proposed for FBP reconstruction and strategies optimal for FBP are suboptimal and may even reduce performance when applied to MBIR. The task-driven imaging framework offers a promising approach for optimizing acquisition and reconstruction for MBIR that can improve imaging performance and/or dose utilization beyond conventional imaging strategies.

Keywords

task-driven imaging; imaging task; detectability index; CT; optimization; tube current modulation; regularization design; model-based iterative reconstruction; image quality

A Introduction

Tube current modulation (TCM) is routinely used on diagnostic CT scanners to reduce radiation dose while maintaining image quality (Kalra *et al* 2004, McCollough *et al* 2009). TCM techniques tend to include modulation along the axial direction and/or modulation as a function of rotation angle. With conventional modulation schemes, lower tube current (and hence less total fluence) is delivered to less attenuating sections of the patient (e.g., chest as compared to shoulders) where lower dose is required to achieve the desired image quality. Moreover, angular modulation is often applied for anatomical sections that have significant variation in thickness as a function of rotation – e.g. for abdominal CT, tube current is usually increased for lateral views and decreased for views along the anterior-posterior axis. Optimal angular TCM pattern poses an interesting design question and requires the adoption of a specific image quality objective. Conventional modulation schemes generally consider a performance metric based on noise and have been designed for CT reconstructions using the filtered-backprojection (FBP) algorithm. For example, one can target uniform signal/noise at the center of the detector by specifying a fluence inversely proportional to the transmissivity (Kalra *et al* 2004). Gies et al. (Gies *et al* 1999) and Harpen (Harpen 1999) directly minimized variance (from quantum noise) at a particular voxel in a FBP reconstruction through a TCM pattern that is proportional to the square root of the transmissivity.

Recent years have seen rapid development and clinical translation of model-based iterative reconstruction (MBIR) algorithms as well as more sophisticated metrics of imaging performance suggesting that TCM design should be revisited. Model-based iterative reconstruction approaches present distinct noise and resolution tradeoffs from FBP. In particular, TCM substantially affects the noise properties in FBP reconstruction but has little effect on the spatial resolution; however, in MBIR, TCM has the potential to affect both noise and resolution in an object-dependent fashion. Therefore, it is unclear whether traditional modulation strategies designed for FBP are optimal for MBIR. Furthermore, there is increasing consensus that image quality quantification needs to move beyond simple metrics of noise and resolution, and must be defined with respect to a particular imaging task (Wagner and Weaver 1972, Barrett 2009, Sharp *et al* 1996). Task-based metrics (e.g., detectability index for a detection task) has been commonly used in image quality assessment (Sharp *et al* 1996), and have found applications in the optimization of various aspects of the imaging system as well (Chawla *et al* 2008, Frey *et al* 2002, Rolland *et al* 2005, Sanchez *et al* 2014, Prakash *et al* 2011, Gang *et al* 2012). Motivated by the above two reasons, we aim to investigate in this work TCM strategies optimal for MBIR consistent with a task-based image quality objective.

Toward this end, we adopt a task-driven imaging framework for prospective optimization of acquisition and reconstruction based on an image quality objective that seeks to maximize the detectability index for a specified imaging task and patient anatomy. The concept of the framework is somewhat similar to adaptive imaging techniques that have been proposed for MRI (Cao and Levin 1993) or SPECT (Barrett *et al* 2008). For CT or cone-beam CT (CBCT), this framework has been used to identify optimal acquisition trajectories in robotic c-arm systems (Stayman and Siewerdsen 2012), as well as TCM, view-dependent

apodization kernels, and orbital tilt for FBP reconstruction (Gang *et al* 2015). In particular relevance to TCM, we derived the optimal modulation pattern in FBP reconstruction that maximizes detectability index for a range of imaging tasks while taking into account a complete system model including system blur, quantum and electronics noise (Gang *et al* 2015). It was found that the optimal TCM for radially symmetric task functions are comparable to the minimum variance solution proposed by Gies et al. (Gies *et al* 1999), while that for asymmetric tasks are strongly dependent on the radial frequency of the task function.

Finding optimal TCM approaches for MBIR presents a number of challenges. MBIR algorithms are typically nonlinear and often lack an explicit closed-form expression of the reconstruction as a function of the measurements. In addition, MBIR methods can present images with significant shift-variance in spatial resolution properties and nonstationarity in noise (Fessler and Rogers 1996, Fessler 1996). These properties are object- and acquisition-dependent, and are also closely tied to the form of regularization or penalty that is integrated into the MBIR algorithm. Many different regularization functions are available, permitting significant freedom in shaping the noise and resolution in the reconstruction. It is likely that the effects of TCM and regularization are coupled. Joint optimization will therefore be potentially important for maximizing imaging performance.

Despite these challenges of nonlinearity and scan-specific dependencies, prospective predictors of imaging performance have been derived for specific MBIR objective functions. In particular, for penalized-likelihood reconstruction, closed-form expressions for local point spread functions and local covariance have been derived even though the estimator itself is implicitly defined (Fessler 1996, Fessler and Rogers 1996). While these expressions generally involve solving a problem with the same computational complexity of an ordinary reconstruction, Fourier approximations have been applied (Stayman and Fessler 2004, Jinyi Qi and Leahy 2000) to permit fast computation of these predictors or their transforms – the local modulation transfer function (MTF) and local noise power spectrum (NPS) – which can, in turn, be used to compute local detectability index. Recently, more efficient closed-form analytical expressions have been derived (Zhang-O'Connor and Fessler 2007, Schmitt and Fessler 2012) permitting even faster computation. Such local and efficient predictors relate imaging parameters to task-based imaging performance and are essential in a computationally feasible parameter optimization of MBIR. Task-based optimization of MBIR has been performed for directional penalty design in emission imaging (Qi and Huesman 2006, Yang *et al* 2014). In transmission tomography, Gang et al. (Gang *et al* 2011) proposed methods for a spatially-varying penalty strength map to maximize task-based detectability index. Schmitt (Schmitt 2015) examined an exhaustive search method for jointly optimizing penalty strength and TCM parameterized by a sinusoid.

In this work, we investigate the joint optimization of TCM and MBIR regularization. Specifically, we extend the task-driven framework for the optimization of angular TCM using a general basis decomposition and a regularizer specified by overall penalty strength as well as the variation of individual pairwise voxel penalties to permit directional control of noise and resolution. We explore optimal design in the context of quadratic penalized-

likelihood reconstruction for a mid-frequency discrimination task in an abdomen phantom, and compare task-driven strategies to conventional TCM and regularization approaches.

B Methods

B.1 Overview of Design Framework

Following previous work (Gang *et al* 2015, Stayman and Siewerdsen 2012), we introduce a task-driven imaging framework for prospective optimization of image acquisition and reconstruction using a task-based objective function. Specifically, the objective function seeks to maximize detectability index – a task-based image quality metric commonly used for performance assessment of classification tasks (detection or discrimination). Detectability index is dependent on the imaging task, the observer model, as well as the noise and resolution characteristics in the reconstruction. Thus, a model of the entire imaging chain is required to predict reconstructed image properties as a function of the patient attenuation characteristics (based on an anatomical model), and the particular acquisition parameters (denoted as Ω_A) and reconstruction parameters (denoted as Ω_R) to be designed. An optimization algorithm is applied that seeks the combination of $(\Omega_{\mathrm{A}}^*, \Omega_R^*)$ that maximizes the objective.

The utility of this framework has been demonstrated primarily in the context of interventional imaging where an anatomical model is typically available in the form of a pre-operative or planning CT study (Gang *et al* 2015, Stayman and Siewerdsen 2012). To adopt the framework in diagnostic CT imaging scenarios, the anatomical model can be derived from a very-low dose 3D scout which replaces the traditional anterior-posterior (AP) and lateral radiographs (Yin *et al* 2015, Gomez *et al* 2017). Specification of the task function can be based on suspected lesions or disease prevalence, and may include multiple tasks. The location of the imaging task may include a single point, one or more organs, or the entire image volume (Gang *et al* 2016).

In this work, we focus on the joint optimization of TCM and regularization at a single, known location for a known imaging task in penalized-likelihood reconstruction with a quadratic penalty. Performing a single location optimization reduces the complexity of the problem and provides basic understanding of how acquisition and reconstruction parameters jointly affect task-based image quality metrics in MBIR. The optimal modulation pattern is dependent on the local spatial resolution and noise properties and is therefore location-dependent. Prescribing optimal fluence patterns for many locations requires additional flexibility in data acquisition – e.g, dynamic fluence field modulation (Stayman *et al* 2016, Hsieh and Pelc 2013, Szczykutowicz and Mistretta 2014, Bartolac *et al* 2011, Gang *et al* 2016) – which is the subject of ongoing investigation.

B.1.1 Task-Driven Objective—For the following investigations, the imaging task is assumed to be a binary classification task (detection or discrimination) presuming a signal-known-exactly and background-known-exactly scenario. A non-prewhitening (NPW) observer model was adopted as a quasi-ideal observer that quantifies the upper bound of imaging performance while modeling the human observer as unable to prewhiten correlated noise. In this case, one may write the local detectability index at voxel *j* as:

$$d_j'^2(\Omega_A,\Omega_R)=\frac{\left[\int\int\int T_j^2(\Omega_A,\Omega_R)W_{Task}^2 df_x df_y df_z\right]^2}{\int\int\int S_j(\Omega_A,\Omega_R)T_j^2(\Omega_A,\Omega_R)W_{Task}^2 df_x df_y df_z}. \quad (1)$$

where f_x, f_y, f_z are frequency axis along the x, y, z axes. This expression is a function of local spatial resolution and noise, expressed in the Fourier domain as the MTF (denoted T) and NPS (denoted S), respectively. This model presumes a linear, shift-invariant (LSI) system and stationary noise within a local neighborhood around voxel j (Gang *et al* 2014). The task function W_{Task}, is equal to the Fourier transform of the difference between binary hypotheses (e.g., signal present versus signal absent for a detection task, or signal under hypothesis 1, H_1, versus signal under hypothesis 2, H_2, for a discrimination task). Focusing on the optimization of imaging performance at a single location, one may directly use the local detectability index as the objective function, i.e.:

$$(\Omega_A^*,\Omega_R^*)=argmax\ d_j'^2(\Omega_A,\Omega_R) \quad (2)$$

While this paper concentrates on the above objective, it is straightforward to generalize design for regional objectives – e.g., based on maximizing the minimum detectability over many locations (Gang *et al* 2016).

B.1.2 Penalized-Likelihood Reconstruction with Quadratic Penalty—The MBIR method investigated in this work is based on a penalized-likelihood (PL) objective with a quadratic roughness penalty. This estimator integrates a statistically motivated data fit term and regularization term to achieve favorable noise-resolution trade-offs and locally linearizable imaging properties for which the locally shift-invariant approximation is accurate (Fessler 1996). The reconstruction, $\hat{\mu}$, is given by:

$$\hat{\mu}=\text{argmax}_\mu[\log L(\mu,y)-R(\mu)] \quad (3)$$

where the vector μ is the volume of attenuation values, the vector y denotes the projection data, $L(\mu, y)$ is the log-likelihood function and $R(\mu)$ is the roughness penalty. In this work, a simplified forward model was adopted assuming an ideal detector with no detector blur, zero electronics noise, and unity gain. Thus, the measurements, y, are a vector of independent Poisson random variables, with means given by:

$$\overline{y}=I_0(\theta)e^{-\mathbf{A}\mu} \quad (4)$$

where **A** is the forward projection operator and I_0 is the number of barebeam photons per detector pixel. Fluence variations achieved via tube current modulation are accounted for in the I_0 term as a function of projection angle, θ.

The quadratic roughness penalty takes the following generalized form:

$$R(\mu)=\sum_j \beta_j \sum_{k\in\mathcal{N}_j} r_{jk}\xi_{jk}\frac{1}{2}(\mu_j-\mu_k)^2 \quad (5)$$

where subscripts j and k denotes voxel locations. The symbol $\mathcal{N}_j$ denotes the neighborhood around voxel where the penalty function is effective. As illustrated in Fig.1, we adopt a neighborhood with eight neighboring voxels in-plane and two neighboring voxels out-of-plane. Note that the size of the neighborhood is usually dependent on user choice and typically involves 1st order neighbors along x, y, and z. The neighborhood in this work was chosen to include voxels that significantly affect the anisotropy of MTF and NPS in the axial plane ($f_x - f_y$). These neighbors would arguably have the most interesting interactions with the effect of tube current modulation, which also manifests mainly in the axial plane. Expanding the neighborhood to higher order neighbors both in- and out-of-plane may be considered for future work.

The terms ξ_{jk} denotes the intrinsic weighting factor based on the distance between voxels j and k. For the neighborhood above, ξ_{jk} is 1 for neighbors along the x, y, and z axes, and $\frac{1}{\sqrt{2}}$ for in-plane diagonal neighbors. Two additional weighting factors, β_j and r_{jk}, control the strength of the penalty. The penalty strength parameter, β_j, determines the overall weight of the penalty term relative to the data fit term. The subscript, j, denotes the general case where the penalty strength can be spatially varying as a function of voxel locations (Stayman and Fessler 2000). The term, r_{jk}, is usually 1 for all voxel pairs in conventional weighting schemes. In this work, r_{jk} is allowed to vary in order to control the strength of the roughness penalty in different directions. This enables additional freedom in shaping the isotropy/anisotropy of the noise and resolution characteristics in the reconstructed image. While ξ_{jk}, r_{jk} and β_j can be mathematically reduced to a single weighting factor, the form in Eq.(5) enables the separate investigation of two aspects of penalty design, i.e., the overall smoothness/sharpness controlled by β_j and the directionality of the noise or resolution controlled by r_{jk} as compared to traditional directional weighting based only on distance (ξ_{jk}).

B.1.3 Acquisition Parameters—For TCM optimization, we consider a circular scanning geometry where the fluence varies simply as a function of rotation angle, i.e., $I_0(\theta)$. Instead of optimizing over all angular positions – a potentially difficult non-convex and high-dimensional estimation problem, we specify a low-dimensional parameterization of the modulation pattern as a linear combination of basis functions, $\mathcal{B}_n(\theta)$:

$$I_0(\theta)=\sum_1^N \Omega_n \mathcal{B}_n(\theta) \quad \text{for } \theta\in[0,2\pi]. \quad (6)$$

where $[\Omega_1, \Omega_2, \ldots, \Omega_N]$ denotes the low-dimensional vector of basis coefficients to be estimated. We choose a set of bases defined by a shifted Gaussian function, $\mathcal{N}_{\theta_n,\sigma}(\theta)$, where

θ_n and σ denote the mean and standard deviation of the Gaussian, respectively. The centers (θ_n) of the Gaussians are evenly spaced along θ. The width of each Gaussian (2σ) is the same for all basis functions, and is chosen such that the value at the mid-point between centers sums to the same as that at the centers such that a flat profile can be achieved by this parameterization. Furthermore, projections 180° apart are redundant under a parallel beam assumption and are therefore assigned the same fluence to further reduce the dimensionality of the parameter. Thus, each basis function is given by:

$$\mathscr{B}_n(\theta)=\sum_{j=0}^{2}\mathscr{N}(\theta_n+j\pi,\sigma)=\sum_{j=0}^{2}\exp\left[\frac{-(\theta_n+j\pi)^2}{2\sigma^2}\right] \quad (7)$$

where

$$[\theta_1,\theta_2,\theta_3,\ldots,\theta_N]=\left[0,\frac{\pi}{N},\frac{2\pi}{N},\ldots,\frac{(N-1)\pi}{N}\right] \text{ and } \sigma=\frac{0.66\pi}{N} \text{ for } \theta\in[0,2\pi].$$

The number of basis functions (N) affects the smoothness of tube current variations over θ. The number should be large enough to allow flexible modulation profiles that capture realistic anatomical variations, but smaller enough to ensure a low-dimensional search and to avoid high-frequency fluctuations that are unachievable by a real CT system. In this work we have chosen N = 8 to such that TCM may vary every ~20^o. An important consideration in choosing the low dimensional parameterization is that it should be versatile enough to represent different classes of modulation profiles so that they are not excluded from the search space. Two conventionally adopted modulation patterns – a constant and a sine squared function - are shown in Fig. 2(b) to illustrate the difference between the basis function representations (solid line) versus ground truth (dashed red line). The two curves overlap almost completely for both modulation patterns, with a root mean square error of ~0.0052% of the mean fluence for the constant pattern and ~0.11% for the sinusoidal pattern.

Various TCM strategies were investigated in this work. To ensure fair comparisons among strategies, a fluence constraint was applied such that the total bare beam fluence for all modulation patterns sum to a constant:

$$\sum_{\theta}I_0(\theta)=I_0^{tot} \quad (8)$$

In addition, a lower bound was applied to the fluence in each projection to constrain the amplitude of modulation. The maximum ratio between the maximum and minimum levels of $I_0(\theta)$ in current clinical CT systems is typically limited (e.g. to a factor of 3) based on x-ray tube and generator capabilities. The above two constraints were achieved through the following variable transformation and the following equation was used in the optimization process:

$$I_0(\theta)=I_0^{\min}+\frac{\sum_1^N \Omega_n \mathscr{B}_n(\theta)}{\sum_\theta \sum_1^N \Omega_n \mathscr{B}_n(\theta)}(I_0^{tot}-\sum_\theta I_0^{min}) \quad (9)$$

B.1.4 Reconstruction Parameters—In addition to TCM, task-driven optimization of the penalty term was also investigated. Using the quadratic penalty form in Eq.(5), we choose r_{jk} and β_j as the design parameters. Similar to TCM, the regularization was optimized for a single location, i.e., a scalar β_j and directional r_{jk} weights for a single voxel, and applied everywhere in the image. For more a general optimization involving multiple locations, spatially varying r_{jk} and β_j can be optimized and applied instead (Fessler and Rogers 1996, Stayman and Fessler 2000, Gang *et al* 2014). As mentioned in Sec.B.1.2, Eq. (5) is redundantly parameterized. To avoid ambiguities in optimization, we apply an additional constraint. Specifically, we chose to normalize the directional penalty weights such that the base-10 logarithm exponents sums up to 0,

$$\sum_k \log_{10} r_{jk}=0. \quad (10)$$

This constraint keeps the overall smoothing relatively constant (recognizing that the weights have logarithmic action due to the log-likelihood objective). Specifically, if r_{jk} is increased in one direction, the weighting for another direction or other directions have to decrease to keep the overall smoothing similar. Additionally, we constrain the maximum allowed variation in r_{jk} to one order of magnitude, i.e., 10 or 1/10. Only the four in-plane (x–y) penalty weights illustrated in Fig.1 were optimized in this work. The r_{jk} in the z-direction is fixed to 1.

B.1.5 Local Noise and Resolution Predictors—The local covariance and point spread function for PL reconstruction was derived by Fessler (Fessler 1996, Fessler and Rogers 1996) based on the implicit function theorem and first-order Taylor expansions. This method, although accurate, involves the iterative estimation of three matrix inverses for each evaluation of d' and thus would be computationally infeasible for incorporation into the optimization framework. Adopting the Fourier approximations in (Stayman and Fessler 2004) permits one to write closed form expressions without any matrix inverses. Specifically, we may write the local MTF and NPS at voxel j as:

$$T_j \approx \frac{|\mathscr{F}\{\mathbf{A}^T\mathbf{W}\mathbf{A}e_j\}|}{|\mathscr{F}\{\mathbf{A}^T\mathbf{W}\mathbf{A}e_j\}+\mathscr{F}\{\mathbf{R}e_j\}|} \quad 11(a)$$

$$S_j \approx \frac{|\mathscr{F}\{\mathbf{A}^T\mathbf{W}\mathbf{A}e_j\}|}{|\mathscr{F}\{\mathbf{A}^T\mathbf{W}\mathbf{A}e_j\}+\mathscr{F}\{\mathbf{R}e_j\}|^2} \quad 11(b)$$

where $\mathscr{F}\{\cdot\}$ denotes the discrete Fourier transform, $\mathbf{A}^T\mathbf{W}\mathbf{A}$ is the Hessian of the data-fit term, $\mathbf{R}$ is the Hessian of the quadratic penalty term, e_j and is a unit vector that is 1 at the voxel location and 0 everywhere else. For transmission tomography with independent Poisson noise, $\mathbf{W}$ can be approximated by $D\{\overline{y}\}$ (Zhang-O'Connor and Fessler 2007) where $D\{\cdot\}$ denotes a diagonal matrix with its vector input as the diagonal elements. Note that dependence on the patient anatomy and TCM strategy is determined through the $\mathbf{W}=D\{\overline{y}\}$ term which is a function of the mean measurements; the dependence on regularization design enters through $\mathbf{R}$ the term.

During the optimization process, we need to repeatedly evaluate Eqs. 11(a) and (b). For fast and memory-efficient computation of $\mathscr{F}\{\mathbf{A}^T\mathbf{W}\mathbf{A}e_j\}$, the following techniques were adopted. First, for each projection angle θ, $\mathscr{F}\{\mathbf{A}_\theta^T\mathbf{A}_\theta e_j\}$ was precomputed numerically and stored. This technique assumes that $\mathbf{W}$ varies slowly on the detector and allows the weighting term for voxel j at projection angle θ (denoted as $w_{j,\theta}$) to be multiplied directly and summed over angles:

$$\mathscr{F}\{\mathbf{A}^T\mathbf{W}\mathbf{A}e_j\}=\sum_\theta w_{j,\theta}\mathscr{F}\{\mathbf{A}_\theta^T\mathbf{A}_\theta e_j\} \quad (12)$$

Thus, only one set of $\mathscr{F}\{\mathbf{A}_\theta^T\mathbf{A}_\theta e_j\}$ over θ needs to be precomputed to achieve any arbitrary TCM patterns.

Second, instead of using the full image support, only a 49×49×49 voxel volume of interest (VOI) centered at voxel j was extracted from $\mathbf{A}_\theta^T\mathbf{A}_\theta e_j$ and used to compute the Fourier approximation in Eq.(11). The VOI size was sufficiently large to capture the $1/r$ blur induced by the $\mathbf{A}_\theta^T\mathbf{A}_\theta e_j$. Thus, voxels values outside of the VOI are 0, and the resulting Fourier transform is more coarsely sampled but retains the same frequency content. Using $(\cdot)^{\mathscr{N}_j'}$ to denote the VOI around voxel j, this technique is represented mathematically as:

$$\mathscr{F}\left\{(\mathbf{A}^T\mathbf{W}\mathbf{A}e_j)^{\mathscr{N}_j'}\right\}=\sum_\theta w_{j,\theta}\mathscr{F}\left\{(\mathbf{A}_\theta^T\mathbf{A}_\theta e_j)^{\mathscr{N}_j'}\right\} \quad (13)$$

Similar techniques were used for the evaluation of $\mathscr{F}\{\mathbf{R}e_j\}$. From derivations in (Zhang-O'Connor and Fessler 2007), $\mathscr{F}\{\mathbf{R}e_j\}$ can be computed analytically as:

$$\mathscr{F}\{\mathbf{R}\}_j(\rho,\phi)=\beta_j\sum_k r_{jk}\xi_{jk}a^3 4\sin^2(\pi a\rho\,\overrightarrow{e}_\phi\cdot\overrightarrow{m}_k) \quad (14)$$

where (ρ, ϕ) is the polar coordinates of the frequency domain, a is the voxel size (assuming isotropic voxel size along x, y, and z), $\overrightarrow{e}_\phi$ is the cartesian unit vector corresponding to the polar unit vector $(1, \phi)$, and $\overrightarrow{m}_k$ is the Cartesian vector of spatial offset from voxel j to voxel

k. For the local penalty design investigated in this work, $\mathscr{F}\{\mathbf{R}e_j\}$ is only dependent on β_j and r_{jk}. Therefore, for efficient implementation, four matrices corresponding to the unweighted frequency response for each penalty direction, $\mathscr{R}_k(\rho,\theta)=\xi_{jk}a^3 4\sin^2(\pi a\rho\overrightarrow{e}_\phi\cdot\overrightarrow{m}_k)$, were precomputed and stored, allowing fast computations of $\mathscr{F}\{\mathbf{R}e_j\}$ for arbitrary β_j and r_{jk}. Again, a 49×49×49 voxel VOI was used instead of the full image support.

B.1.6 Imaging Strategies and Optimizer—Six imaging strategies were investigated and compared using PL reconstruction, including both conventional TCM techniques and task-driven TCM and penalty design. Various strategies for TCM exist ranging from simple heuristic sinusoids based on the oblateness of the patient, as well as more sophisticated methods calculated as a function of the attenuation characteristics of the patient. In this work, we focus on the latter using the parameterization proposed by Gies et al.(Gies *et al* 1999):

$$I_0(\theta)=\frac{e^{\alpha l}j,\theta}{\sum_n e^{\alpha l}j,\theta}I_{tot} \quad (15)$$

where l_{j,θ_m} denotes the line integral through voxel j at projection angle θ_m and α is a scalar value that controls the amplitude of modulation. We select the following three imaging strategies as traditional TCM choices that have been suggested and used in the context of FBP reconstruction:

Strategy 1: Unmodulated Tube Current (α = 0). The tube current is constant for each projection.

Strategy 2: Uniform Detector Signal (α = 10). When α = 1.0, the fluence incident on the detector for the source-detector ray passing through voxel j is constant for each projection. The statistical weighting for measurements associated with image position j is therefore the same for each projection angle, and one would expect isotropic noise and resolution properties for a likelihood-based reconstruction.

Strategy 3: Minimum Variance in FBP (α = 0.5). From Gies et al., the variance of voxel in an FBP reconstruction is minimized when α = 0.5.

Though these strategies were developed for FBP, they are still being applied to MBIR reconstructions in current clinical protocols. Therefore, we will explicitly evaluate their performance in PL reconstruction. To present a fair evaluation and comparison among strategies, the regularization strength β_j was optimized for each to obtain the highest detectability. For optimization of a local, scalar β_j, an exhaustive search was performed over discrete values of β_j and the optimum was identified to within $\pm 1^{0.03}$. Again, since this work concentrates only on local design, only a single β_j optimization was performed and that β_j value was applied globally as a shift-invariant weight.

The next three strategies follow the task-driven optimization framework and investigate combinations of the image parameters described in Sec.B.1.3 and B.1.4.

Strategy 4: Task-driven $I_0(\theta)$. Task-driven optimization of tube current modulation and β_j.

Strategy 5: Task-driven r_{jk}. Task-driven optimization of directional penalty weights and β_j.

Strategy 6: Task-driven $I_0(\theta) + r_{jk}$. Task-driven optimization of tube current modulation, directional penalty weights, and β_j.

Contrary to Strategies 1–3 which only involve the optimization of β_j, the optimizations for Strategies 4–6 involves a vector input (coefficients of $I_0(\theta)$ and/or r_{jk} in addition to β_j). We adopted the Covariance Matrix Adaptation Evolution Strategy (CMA-ES)(Hansen and Ostermeier 1996) algorithm for these optimizations. The algorithm is stochastic and derivative-free, making it suitable for non-linear, non-convex problems. An open-source Python implementation of the algorithm was obtained from (Hansen 2014) (Hansen and Kern 2004). A population size of 60 was chosen for each iteration. The initial step size was 0.1 and the stopping criterion is based on a function tolerance of 0.001, which is on the order of ~10^{-5} of the final objective function value.

B.2 Experimental Methods

B.2.1 Imaging Phantoms and Tasks—The six imaging strategies described in Sec.1.6 were investigated in a digital abdomen phantom [Fig.3(a)] derived from the reconstructed CT image of a cadaver torso. To generate the phantom, the CT reconstruction was segmented into air, soft tissue, liver/kidney, and bone. The first three tissue types in the segmented image were assigned a homogeneous value equal to the mean voxel values in a corresponding region of interest (ROI): air 0 mm^{-1}, soft-tissue 0.173 mm^{-1}, liver/kidney 0.019 mm^{-1}. Bone details and attenuation values were preserved from the original data. The voxel size of the digital phantom was 0.871×0.871×0.871 mm.

The imaging task was formulated as the discrimination of a calcification cluster (hypothesis H_1) from a monolithic calcification (hypothesis H_2) shown in Fig.3(b). The calcification cluster consists of three rotationally symmetric Gaussian functions (standard deviation = 1.0 mm) evenly distributed along the perimeter of a 3.3 mm radius circle. The contrast of each Gaussian was 0.024 mm^{-1} relative to the soft tissue background. The larger monolithic calcification was modeled as a Gaussian function rotationally symmetric in the x–y plane with its 50% value equal to the radius of the circle (3.3 mm). Its standard deviation in the z-axis is equal to that of the smaller Gaussians (1.0 mm). We assumed that all axial-rotational orientations of the cluster are equally likely and accounted for this effect numerically by averaging Fourier transform of the cluster rotated at every 2° increment. The Fourier transform of the larger Gaussian was then subtracted to obtain the task function. Mathematically,

$$W_{Task} = \int_\theta \mathcal{F}\{\mu_1^{true}(\theta)\} - \mathcal{F}\{\mu_2^{true}\} \approx \sum_\theta \mathcal{F}\{\mu_1^{true}(\theta)\} - \mathcal{F}\{\mu_2^{true}\} \quad (16)$$

where μ^{true} denotes the true object and is to be distinguished from the reconstruction $\hat{\mu}$. The resulting task function is rotationally symmetric in f_x–f_y and is plotted in Fig.3(c).

To gain further intuition on the task-driven design, we explicitly explored the relationship between regularization and optimal tube current modulation. Using the CMA-ES algorithm, the optimal $I_0(\theta)$ was identified at fixed values of β_j in a simplified phantom using idealized imaging tasks. Specifically a homogeneous ellipse phantom (major axis ≈ 90 mm, minor axis ≈ 60 mm) with the task location at the center as illustrated in Fig.3(d) was employed. Three task functions were constructed for the detection of low-, mid-, and high-frequency content [Fig.3(e)]. The low frequency task was the Fourier transform of a Gaussian of standard deviation 3 mm. The mid- and high-frequency tasks were formulated directly in the Fourier domain as the difference between two Gaussians. For the mid-frequency task, the standard deviation of the two Gaussians are 0.25 mm^{-1} and 0.15 mm^{-1}; for the high-frequency task, 0.40 mm^{-1} and 0.35 mm^{-1}. Values of β_j spanned 5 orders of magnitude from 10 to 10^6.

B.2.2 Image Simulation and Reconstruction—Projections were simulated at a pixel pitch of 1.17×1.17 mm to match the voxel size (times the magnification factor) for the digital phantom. The nominal exposure level is 750 photons per pixel (or ~548 photons per mm^2) per projection, giving a total fluence of ~1.97×10^5 photons per mm^2 for the entire acquisition. This low dose simulation was used to provide a challenging scenario for the different imaging strategies to yield performance differences that can be appreciated visually. The lower limit of fluence in Eq.9 is 450 photons per pixel. Efficient GPU-based implementations of the forward- and back-projectors using the Siddon algorithm (Siddon 1985) were adopted. Poisson noise was generated using the *random.poisson* function in the Numpy package. The system geometry used a source-axis-distance of 804 mm and a source-detector-distance of 1080 mm.

Penalized-likelihood reconstructions were performed using Nesterov momentum updates and ordered subsets for acceleration (Kim *et al* 2013). A total of 60 iterations were performed, with 20 subsets for the first 30 iterations and 1 subset for the last 30 iterations to ensure convergence. Reconstruction voxel size was the same as that of the digital phantom (0.871×0.871×0.871 mm).

B.2.3 Validation of Theoretical Predictions of MTF and NPS—The MTF and NPS from theoretical predictions (calculated according to Sec.B.1.5) were validated with empirical calculations. For NPS, 50 repeated reconstructions were performed and the difference image for each image pair was computed. The NPS was then calculated as the ensemble average of the square of the Fourier transform of a 49×49×49 voxel VOI around the location of the imaging task (denoted by j) in each difference image, i.e.,

$$S(f_x, f_y, f_z) = \frac{1}{2}\frac{a_x a_y a_z}{n_x n_y n_z}\left\langle \left| \mathscr{F}\left\{ \Delta^{N_j'}(x,y,z) \right\} \right|^2 \right\rangle \quad (17)$$

Using $(\cdot)^{\mathcal{N}_j'}$ to denote the VOI around voxel *j*, where denotes a difference image, $\mathcal{N}_j'$ is the neighborhood notation consistent with Eq.(13), a_x is the voxel size, n_x is the number of voxels along the *x*-direction, and the $\frac{1}{2}$ accounts for noise amplification from the subtraction process. For MTF, the local impulse response was first computed as the magnitude-normalized difference between mean reconstructions of the true object with and without an impulse (amplitude $\delta = 0.01\text{mm}^{-1}$) injected at the location of interest. The MTF was then calculated as the modulus of the Fourier transform of the impulse response function within a 49×49×49 voxel volume of interest around the location of the impulse, i.e.,

$$T(f_x, f_y, f_z) = \mathscr{F}\left\{ \left(\frac{\hat{\mu}[\overline{y}(\mu^{true}) - \hat{\mu}[\overline{y}(\mu^{true} + \delta e_j)]}{\delta} \right)^{\mathcal{N}_j} \right\} \quad (18)$$

B.2.4 Visual Illustration of Image Quality—Example reconstructions from the six imaging strategies were presented for purposes of illustration. In low dose imaging scenarios, individual noise realizations can have a substantial impact on the appearance of the signal. Therefore, showing a single arbitrary reconstruction from each imaging strategy may not be representative of image quality. Instead, we developed a method rooted in statistical decision theory for fair selection of reconstructions from an ensemble. Note that the example images are only meant to serve as "visual aids" for the d' values. Definitive performance comparisons should only be concluded from observer studies which will be subjects of future work.

For each imaging strategy, we generated noisy data and reconstructed 50 realizations for a digital phantom containing the stimulus – in this case, the calcification cluster described in Sec.B.2.1. The test-statistics corresponding to this hypothesis, t_1, was computed for each realization according to

$$t_1 = m^{\mathbf{T}}\hat{\mu}_1 = (\overline{\hat{\mu}} - \overline{\hat{\mu}}_2)^{\mathbf{T}}\hat{\mu}_1 \quad (19)$$

where m denotes the template vector for an NPW observer and is equal to the difference between the mean reconstruction vectors of the two signals under each hypothesis, $\overline{\hat{\mu}}_1 - \overline{\hat{\mu}}_2$. The mean reconstruction was approximated from reconstruction of noiseless data for the two hypotheses (H_1–calcification cluster, and H_2–"monolithic" Gaussian). The support of the template was chosen to be a 29×29×9 voxel VOI centered at the location of the signal.

Particular noise realizations that are particularly bad (or good) for the specific discrimination task can be graded and identified using Eq. (19). To do so, the values of t for each reconstruction method ensemble is ordered and reconstructions closest to particular percentile values were selected from each imaging strategy for comparison. Specifically, we identified and presented the reconstructions at 100^{th} (best case), 80^{th}, 50^{th}, and 20^{th} percentiles for each strategy in Sec.C.2 below.

C Results

C.1 Comparison of Imaging Strategies

A summary of the imaging parameters associated with each of the six imaging strategies described in Sec.B.1.6 are shown in Figure 4 including (a) TCM, $I_0(\theta)$, (b) directional penalty weights, r_{jk}, and (c) overall penalty strength β_j. Tube current modulation is shown as polar plot and overlaid on the abdomen phantom in the Unmodulated strategy to help illustrate the dependence on patient anatomy. In the Uniform Signal ($\alpha = 1.0$) case, more fluence is allocated to the more highly attenuating lateral views so as to homogenize fluence in all views at the detector location corresponding to the stimulus location. The Min. FBP Variance ($\alpha = 0.5$) case is the square root of the Uniform Signal ($\alpha = 1.0$) case and therefore has smaller amplitude but similarly shaped modulation. Both task-driven designs of tube current modulation (i.e., Task-Driven $I_0(\theta)$ and Task-Driven $I_0(\theta) + r_{jk}$), on the other hand, have the opposite trend where the highest fluence levels were assigned to the least attenuating views along the anterior-posterior (AP) axis. The lowest fluence levels for the two strategies are along the lateral views and are limited by the constraint placed on the optimization [$I_0^{\min}$ in Eq.(9)]. The maximum ratio between the maximum and minimum levels of $I_0(\theta)$ is ~3.0 and ~3.3 for the Task-Driven $I_0(\theta)$ and Task-Driven $I_0(\theta) + r_{jk}$ strategies, respectively, and is consistent with the tube current dynamic range achievable on modern CT scanners.

Directional penalty weights, r_{jk}, [Fig. 4(b)] are presented with their base-10 logarithmic values. Both task-driven strategies apply greater smoothing along the y-axis and the 45° diagonal, and less smoothing along and the 135° diagonal. Note that smoothing along y-axis in the image domain corresponds to smoothing in f_y which in turn corresponds to lateral views at 90°. Therefore, greater smoothing is applied to data from projections with lower fluence. The penalty strength parameter, β_j, [Fig 4(c)] varies among the imaging strategies by ~ three orders of magnitude, with the lowest β_j observed for $\alpha = 1.0$ and highest for the Task-Driven $I_0(\theta)$ strategy.

The local MTF and NPS at the location of the signal is shown in Fig.5. Theoretical predictions are shown on the upper half and empirical calculations from the 50 reconstructions are shown on the bottom half. Good agreement between theoretical prediction and empirical calculations are obtained in all cases. To provide quantification of the level of agreement, the Pearson correlation coefficient between three radial profiles (horizontal, vertical, and diagonal) of the theoretical and empirical MTF and NPS were computed for all six profiles. The level of agreement are comparable among strategies, with

the mean correlation coefficient for MTF equal to 0.9983±0.0013 and that for NPS 0.9432±0.0345.

The Unmodulated strategy shows the intrinsic noise-resolution tradeoff in PL reconstruction, where noisier data along the lateral direction (contributing to frequencies along f_y) are smoothed more. The Uniform Signal ($\alpha = 1.0$) strategy results in the same weighting for each view and, hence, no preferential smoothing for different orientations. Thus, the MTF and NPS are isotropic. The Min. FBP Variance ($\alpha = 0.5$) strategy yields MTF and NPS results qualitatively "in between" the unmodulated and the Uniform Signal ($\alpha = 1.0$) cases. The three task-driven strategies accentuate the intrinsic anisotropy of MTF and NPS, with the combined Task-Driven $I_0(\theta) + r_{jk}$ optimization yielding the most directional MTF and NPS.

The trend in MTF helps to explain the difference in orders of magnitude of β. Intuitively, the MTF that are optimal for d' would match the width of the task function to give the maximum task power [numerator of Eq.(1)] while avoiding excessive noise power that might degrade d'. At their respective β_j values in Fig.4, the MTF for all six strategies has approximately the same *maximum* radial full-width at half-maximum (from Strategies 1–6: 0.26, 0.24, 0.24, 0.26, 0.32, 0.31 mm^{-1}), which approximately encompasses the peak of task function [Fig.3(e)]. Strategies with MTFs that are not as "stretched out" therefore require a lower β_j in order to reach the higher frequencies, such as the Uniform Signal ($\alpha = 1.0$), Min. FBP Variance ($\alpha = 0.5$), and Task-Driven r_{jk} strategies; whereas strategies with very anisotropic MTFs (Task-Driven TCM and Task-Driven TCM + r_{jk}) can reach these high frequencies at a higher β_j as a result of TCM. All three task-driven strategies suggest the same trend – greater fluence is applied to less attenuating views to obtain sharper MTFs that boost task power. Less fluence and therefore noise are concentrated in higher attenuation views where both the estimator itself and additional penalty through r_{jk} are used to apply greater smoothing and reduce noise.

Figure 6 presents the task-driven $I_0(\theta)$ designs at fixed βs for the low-, mid-, and high-frequency tasks [Fig.3(e)] at the center of the ellipse phantom [Fig.3(d)]. Interestingly, when β_j is small, the optimal tube current modulation for all three tasks closely approximates the $\alpha = 0.5$ modulation (superimposed as red dotted lines), i.e., the optimal tube current modulation for PL reconstruction is similar to that for FBP when regularization has negligible effect. As β_j increases, the modulation pattern shifts to similar trends as seen in Fig.4 where more fluence is assigned to less attenuating views at 0° and 180°. The shift occurs at lower β for higher frequency tasks. The optimal β_j (i.e., highest detectability index), indicated by the green circle, is smaller for higher frequency tasks, consistent with intuition that higher spatial resolution is required to optimize performance for a higher frequency task.

C.2 Reconstructed Images for Different Strategies

The test statistic, t, for the calcification cluster (hypothesis H_1) was computed for 50 reconstructions for each imaging scenario. A sample histogram of t is shown as a bar plot in Fig.7(a) for the Task-Driven $I_0(\theta) + r_{jk}$ case. Under the assumption that test statistics follows a Gaussian distribution, a Gaussian fit to the data is superimposed as a solid curve. Similar

histograms for other approaches are not shown. The distribution for the H_2 hypothesis (monolithic Gaussian) – shown (dashed line) only for illustrative purposes was not generated empirically but was presumed to be Gaussian, with its mean equal to the inner product of the template with the noiseless reconstruction of the monolithic Gaussian signal and the same variance as that of the distribution for H_1. As indicated in Fig.7(a), the best case reconstruction of H_1 has a test statistic value that is the furthest away from the distribution of H_2 while the worst reconstruction of H_1 has a test statistic closest to the H_2 curve.

Reconstruction ROIs corresponding to the 100th (best case), 80th, 50th, and 20th percentiles of the respective test statistics distributions are shown for the six imaging strategies (columns) in Fig. 8. A relative d' based on normalization to the Unmodulated strategy, d'_{rel}, is presented along the bottom of the figure. Within each strategy, the ease of performing the imaging task (discrimination between the calcification cluster and the monolithic Gaussian) generally agrees visually with the best to worst ranking suggested by the t value. Comparing across the different strategies, the relative performance of different TCM and regularization approaches is consistent with the computed value of d'_{rel}. Qualitatively, the Task-Driven $I_0(\theta) + r_{jk}$, approach provides the most easily discernable calcification cluster (most evident in the 100th and 80th percentile reconstructions). The next best strategy appears to be Task-Driven $I_0(\theta)$ where the calcification cluster is the most obvious in the 100th percentile reconstruction. For the rest of the imaging strategies, the imaging task is challenging in all four percentiles, with the $\alpha = 1.0$ strategy appearing most noisy and difficult to discriminate between the cluster and monolithic stimulus hypotheses.

D Discussion

This paper presented a prospective, task-driven optimization of tube current modulation and quadratic penalty design in PL reconstruction. For the optimization of imaging performance, the objective function was chosen to be the detectability index of the intended imaging task at a specific location. The method is patient-specific and requires an anatomical model (e.g., from a prior CT image) to provide the attenuation characteristics for determining the location-specific noise and spatial resolution which are necessary for computing detectability index. Tube current modulation was parameterized using a smooth set of basis functions and quadratic penalty parameterization included overall penalty strength as well as directional penalty weights. The optimization was performed for a sample discrimination task of a calcification cluster versus a monolithic lesion in the kidney. Results from task-driven optimization were then compared with conventional strategies that were originally developed for FBP reconstruction.

For the imaging scenarios investigated in this paper, the optimization results suggest a tube current modulation that assigns greater fluence to less attenuating views and less fluence to more highly attenuating views – suggesting that it may be more important to “make good data better”, than “make bad data good”. These results are direct opposite to TCM schemes traditionally applied for FBP reconstruction (e.g., the minimum variance solution when $\alpha = 0.5$). For FDK reconstruction, the amount of smoothing in the image is independent of the incident fluence and maximizing detectability index for a radially symmetric task is

equivalent to minimizing the NPS. In contrast, PL reconstruction assigns a statistical weighting to the projection data (**W** in Eq.4) typically equal to the variance of each measurement. The amount of smoothing is determined by the statistical weighting relative to the penalty term with greater smoothing applied to noisier data. Due to this property, the noise advantage from increasing fluence in a noisy view is less in PL as compared to FBP. In addition, when the penalty term is dominant for noisy data, further decreasing fluence in these views does not result in as much of an increase in noise. In fact, for a fixed total fluence and regularization strength, the variance of a particular voxel of interest in PL is fairly insensitive to tube current modulation. On the other hand, increasing fluence results in a sharper MTF and this effect is greater in less noisy views compared to noisier views. The distinct noise-resolution tradeoff in PL leads to an optimal tube current modulation that is the opposite from that for FBP reconstruction. Thus, as seen in the reconstruction comparisons, the α = 1.0 strategy performs the worst, followed by the and unmodulated strategies. While the α = 1.0 strategy may be suboptimal in terms of detectability index (and the particular task investigated here), isotropic noise and resolution may be important for other tasks.

The trends in directional penalty weights are consistent with that of tube current modulation, where the intrinsic directionality of MTF and NPS is further enhanced. Interestingly, Qi and Heusman (Qi and Huesman 2006) obtained similar trends in emission tomography using a channelized Hotelling observer model with internal noise. In fact, the anisotropic nature of MTF and NPS in the Unmodulated strategy is exaggerated in all three task-driven strategies, with the Task-Driven TCM + r_{jk} strategy presenting the most directional blur in the reconstructed image. While such anisotropy is favored for the purpose of detection/discrimination in this work, other types of imaging tasks (e.g., size estimation) may require more isotropic resolution to preserve the shape of the lesion. Radiologists may also prefer more familiar looking images with less directional correlations. This could be accomplished by constraining the variation in the directional penalty and/or the fluence modulation. The optimal regularization strength parameter (β_j) roughly matches the MTF (and NPS) to the same frequency extent as the imaging task, which results in a difference of ~three orders of magnitude among β_j for different strategies. Another imaging scenario of clinical relevance involves optimizations at matched noise levels. In that case, we may need to investigate a few different noise levels (e.g., optimal noise level for each strategy) to present a fair comparison.

Detectability index computation was performed in the Fourier domain using the local MTF and NPS in a small voxel neighborhood around the location of interest and for small changes in signal magnitude. Due to the slowly-varying nature of the measurement (and thus the data weighting term) as well as the additional smoothing induced by the back-projector (the $\mathbf{A}^T\mathbf{WA}$ term), the input to the reconstruction process may be assumed to be wide-sense stationary and the local impulse response in the image can be assumed to be shift-invariant within a local neighborhood. Furthermore, a locally linear approximation (around the mean measurement) was shown to hold for a PL objective with quadratic penalty (Fessler and Rogers 1996). These assumptions allow the adoption of Fourier domain metrics, which enables fast calculations of d' in the Fourier domain. While it is possible to calculate their

spatial domain counterparts, i.e., point spread function, covariance, and compute d' using a spatial domain version of Eq.1, each set of calculations would require three iterative estimations of matrix inverses which imposes huge computational burden on the optimization processes. Previous work (Gang *et al* 2011) also explicitly examined the validity of such assumptions by comparing the d' values for a Hoteling observer calculated in the Fourier domain vs. those in calculated in the spatial domain. The difference for PL reconstruction with a quadratic penalty was found to be small (~5%) within uniform regions or regions with low contrast structures (e.g., soft tissue to air). Adopting Fourier approximations has the additional benefit of reducing the computation time of the estimators and making the optimization computationally feasible.

The type of regularization studied in this work is quadratic. Other forms of regularization, such as L-1 or Huber penalty, are attractive due to their edge-preserving nature. Optimization involving such penalty function are challenging due to a lack of close-form analytical expression for noise and resolution. For Huber penalty specifically, the quadratic form may still be useful for low contrast signals when the penalty operates in the quadratic region. However, a general analytical approximation would be necessary for high contrast structures. In addition, the local shift-invariance assumption no longer holds around edges and one may need to use the spatial domain calculations mentioned above.

The observer model adopted in this work is the linear non-prewhitening model, chosen as a quasi-ideal model to represent the upper bound of detectability while taking into account of human's inability to prewhiten correlated noise. Inclusion of the non-prewhitening feature is important for this work because prewhitening observers are invariant to the amount of smoothing in the reconstructed image and would not yield an optimum for regularization design. Similarly, prewhitening observers can "undo" correlations introduced by the reconstruction process such that the optimal tube current modulation would assign all the fluence to the least attenuating view for the location of signal (Schmitt 2015). Ideally, the observer model should be one that perfectly matches the human visual response, including characteristics of slice scrolling, search, as well as the effect of non-uniform background. The task-driven imaging framework is sufficiently general to accommodate any form of observer models in the objective function and incorporating the latest development in image perception research will subject of future work.

Several simplifications were invoked in this work and will be addressed in future studies. The forward model in this work assumed an ideal detector with no detector blur, unity gain, and zero electronic noise. Noise and resolution predictors for PL reconstruction with a realistic detector model is the subject of ongoing investigation (Wang *et al* 2017) and will be incorporated in the optimization framework in future studies. The inclusion of detector blur will likely result in a small change in the magnitude of the regularization parameters. The inclusion of electronic noise poses additional considerations on the lower limit of tube current in each view. Additional constraints might be needed to keep the number of incident photons above the electronic noise floor. Alternatively, we may relax the constraint that all views must have non-zero tube current and allow tomosynthesis-like scenarios to occur. In that case, we require a more sophisticated observer model that takes into account of the

effect of overlaying anatomy (viz. increased anatomical noise (Gang *et al* 2010) and reduction in contrast of the stimulus from 3D to 2D) as well as streaking artifacts.

The frequency content and location of the imaging task in this work was assumed to be known exactly. In diagnostic imaging scenarios, a multi-task and multi-location optimization is likely needed to account for a range of possible lesions specific to the anatomical site based on disease prevalence. Results from the single location investigation in this work suggest that the optimal TCM profile is affected by the attenuation characteristics at the location of interest and therefore varies as a function of location. While appropriate for optimization at a single location, one cannot drive arbitrary fluence to many stimuli locations with simple TCM. Multi-location optimization using TCM alone will therefore only be able to consider the most challenging location, or improve average or weighted average performance over all locations. A technology more suited to multi-location optimization is (Stayman *et al* 2016, Szczykutowicz and Mistretta 2014, Hsieh and Pelc 2013, Bartolac *et al* 2011) which generalized the TCM concept to provide varying spatial modulations of the x-ray beam as a function of rotation angle have been developed. Initial studies generalizing the TCM strategies presented here are underway to permit greater freedom in providing locally optimal fluence-field modulation to multiple locations in the image (Gang *et al* 2016).

Acknowledgments

The authors would like to thank Dr. Reuvin Levinson for helpful discussions regarding tube current modulation on commercial CT scanners. This work is supported in part by NIH grant U01EB017858.

References

Barrett, HH. NEQ: its progenitors and progeny. In: Sahiner, B., Manning, DJ., editors. SPIE Medical Imaging. International Society for Optics and Photonics; 2009. p. 72630F-72630F.

Barrett HH, Furenlid LR, Freed M, Hesterman JY, Kupinski MA, Clarkson E, Whitaker MK. Adaptive spect. IEEE Trans Med Imaging. 2008; 27:775–88. [PubMed: 18541485]

Bartolac S, Graham S, Siewerdsen JH, Jaffray D. Fluence field optimization for noise and dose objectives in CT. Med Phys. 2011; 38(Suppl 1):S2. [PubMed: 21978114]

Cao, Y., Levin, DN. Biennial International Conference on Information Processing in Medical Imaging. Springer; Feature-guided acquisition and reconstruction of MR images; p. 278-92.

Chawla AS, Samei E, Saunders RS, Lo JY, Baker JA. A mathematical model platform for optimizing a multiprojection breast imaging system. Med Phys. 2008; 35:1337–45. [PubMed: 18491528]

Fessler JA. Mean and variance of implicitly defined biased estimators (such as penalized maximum likelihood): applications to tomography. IEEE Trans Image Process. 1996; 5:493–506. [PubMed: 18285134]

Fessler JA, Rogers WL. Spatial resolution properties of penalized-likelihood image reconstruction: space-invariant tomographs. Image Process IEEE Trans. 1996; 5:1346–58.

Frey EC, Gilland KL, Tsui BMW. Application of task-based measures of image quality to optimization and evaluation of three-dimensional reconstruction-based compensation methods in myocardial perfusion SPECT. IEEE Trans Med Imaging. 2002; 21:1040–50. [PubMed: 12564872]

Gang GJ, Lee J, Stayman JW, Tward DJ, Zbijweski W, Prince JL, Siewerdsen JH. Analysis of Fourier-domain task-based detectability index in tomosynthesis and cone-beam CT in relation to human observer performance. Med Phys. 2011; 38:1754–68. [PubMed: 21626910]

Gang GJ, Siewerdsen JH, Stayman JW. Task-Based Design of Fluence Field Modulation in CT for Model-Based Iterative Reconstruction. Proceedings of the 4th International Conference on Image Formation in X-Ray Computed Tomography. 2016:407–10.

Gang GJ, Stayman JW, Ehtiati T, Siewerdsen JH. Task-driven image acquisition and reconstruction in cone-beam CT. Phys Med Biol. 2015; 60:3129–50. [PubMed: 25803361]

Gang GJ, Stayman JW, Zbijweski W, Siewerdsen JH. Task-based detectability in CT image reconstruction by filtered backprojection and penalized likelihood estimation. Med Phys. 2014; 41

Gang GJ, Tward DJ, Lee J, Siewerdsen JH. Anatomical background and generalized detectability in tomosynthesis and cone-beam CT. Med Phys. 2010; 37:1948–65. [PubMed: 20527529]

Gang GJ, Zbijweski W, Stayman JW, Siewerdsen JH. Cascaded systems analysis of noise and detectability in dual-energy cone-beam CT. Med Phys. 2012; 39:5145–56. [PubMed: 22894440]

Gies M, Kalender WA, Wolf H, Suess C, Madsen MT. Dose reduction in CT by anatomically adapted tube current modulation. I. Simulation studies. Med Phys. 1999; 26:2235. [PubMed: 10587204]

Gomez J, Gang GJ, Mathews A, Stayman JW. An Investigation of Low-Dose 3D Scout Scans for Computed Tomography. SPIE Medical Imaging. 2017

Hansen N. The CMA Evolution Strategy. 2014

Hansen, N., Kern, S. International Conference on Parallel Problem Solving from Nature. Springer; 2004. Evaluating the CMA evolution strategy on multimodal test functions; p. 282-91.

Hansen, N., Ostermeier, A. Proceedings of IEEE International Conference on Evolutionary Computation. IEEE; 1996. Adapting arbitrary normal mutation distributions in evolution strategies: the covariance matrix adaptation; p. 312-7.

Harpen MD. A simple theorem relating noise and patient dose in computed tomography. Med Phys. 1999; 26:2231. [PubMed: 10587203]

Hsieh SS, Pelc NJ. The feasibility of a piecewise-linear dynamic bowtie filter. Med Phys. 2013; 40:31910.

Jinyi, Qi, Leahy, RM. Resolution and noise properties of MAP reconstruction for fully 3-D PET. IEEE Trans Med Imaging. 2000; 19:493–506. [PubMed: 11021692]

Kalra MKM, Maher MM, Toth TL, Schmidt B, Westerman BL, Morgan HT, Saini S. Techniques and applications of automatic tube current modulation for CT 1. Radiology. 2004; 233:649–57. [PubMed: 15498896]

Kim D, Ramani S, Fessler JA. Accelerating X-ray CT ordered subsets image reconstruction with Nesterov's first-order methods. Proc Intl Mtg on Fully 3D Image Recon in Rad and Nuc Med. 2013:22–5.

McCollough CH, Primak AN, Braun N, Kofler J, Yu L, Christner J. Strategies for Reducing Radiation Dose in CT. Radiol Clin North Am. 2009; 47:27–40. [PubMed: 19195532]

Prakash P, Zbijweski W, Gang GJ, Ding Y, Stayman JW, Yorkston J, Carrino JAA, Siewerdsen JH. Task-based modeling and optimization of a cone-beam CT scanner for musculoskeletal imaging. Med Phys. 2011; 38:5612–29. [PubMed: 21992379]

Qi J, Huesman RH. Penalized maximum-likelihood image reconstruction for lesion detection. Phys Med Biol. 2006; 51:4017. [PubMed: 16885621]

Rolland J, Cheong K-I, Chakrabarti R, Ferris R, Clarkson E, O'Daniel J, Akcay C, DeLemos T, Lee KS. Task-based optimization and performance assessment in optical coherence imaging. JOSA A. 2005; 22:1132–42. [PubMed: 15984486]

Sanchez AA, Sidky EY, Pan X. Task-based optimization of dedicated breast CT via Hotelling observer metrics. Med Phys. 2014; 41:101917. [PubMed: 25281969]

Schmitt, SM. Doctoral dissertation. The University of Michigan; 2015. Fast Variance Prediction for Iteratively Reconstructed CT with Applications to Tube Current Modulation.

Schmitt, SM., Fessler, JA. 2012 IEEE Nuclear Science Symposium and Medical Imaging Conference Record (NSS/MIC). IEEE; 2012. Fast variance computation for quadratically penalized iterative reconstruction of 3D axial CT images; p. 3287-92.

Sharp PF, Metz CE, Wagner RF, Myers KJ, Burgess AE. ICRU Rep. 54 Medical imaging: the assessment of mage quality. Int Comm Radiol Units Meas (Bethesda, Md). 1996

Siddon RL. Fast calculation of the exact radiological path for a three-dimensional CT array. Med Phys. 1985; 12:252. [PubMed: 4000088]

Stayman JW, Fessler JA. Efficient calculation of resolution and covariance for penalized-likelihood reconstruction in fully 3-D SPECT. IEEE Trans Med Imaging. 2004; 23:1543–56. [PubMed: 15575411]

Stayman JW, Fessler JA. Regularization for uniform spatial resolution properties in penalized-likelihood image reconstruction. IEEE Trans Med Imaging. 2000; 19:601–15. [PubMed: 11026463]

Stayman, JW., Mathews, A., Zbijweski, W., Gang, GJ., Siewerdsen, JH., Kawamoto, S., Blevis, I., Levinson, R. SPIE Medical Imaging. International Society for Optics and Photonics; 2016. Fluence-field modulated x-ray CT using multiple aperture devices; p. 97830X-97830X.

Stayman, JW., Siewerdsen, JH. Task-based trajectories in iteratively reconstructed interventional cone-beam CT; Proceedings of 12th International Meeting on Fully Three-Dimensional Image Reconstruction in Radiology and Nuclear Medicine; Lake Tahoe, CA. 2012. p. 257-60.

Szczykutowicz TP, Mistretta CA. Experimental realization of fluence field modulated CT using digital beam attenuation. Phys Med Biol. 2014; 59:1305. [PubMed: 24556823]

Wagner, RF., Weaver, KE. Application of Optical Instrumentation in Medicine. International Society for Optics and Photonics; 1972. An assortment of image quality indexes for radiographic film-screen combinations—can they be resolved?; p. 83-94.

Wang W, Gang GJ, Stayman JW. Spatial resolution properties in penalized-likelihood reconstruction of blurred tomographic data. Fully 3D Meeting. 2017 p Submitted.

Yang L, Zhou J, Ferrero A, Badawi RD, Qi J. Regularization design in penalized maximum-likelihood image reconstruction for lesion detection in 3D PET. Phys Med Biol. 2014; 59:403. [PubMed: 24351981]

Yin Z, Yao Y, Montillo A, Wu M, Edic PM, Kalra M, De Man B. Acquisition, preprocessing, and reconstruction of ultralow dose volumetric CT scout for organ-based CT scan planning. Med Phys. 2015; 42:2730–9. [PubMed: 25979071]

Zhang-O'Connor Y, Fessler JA. Fast predictions of variance images for fan-beam transmission tomography with quadratic regularization. IEEE Trans Med Imaging. 2007; 26:335–46. [PubMed: 17354639]

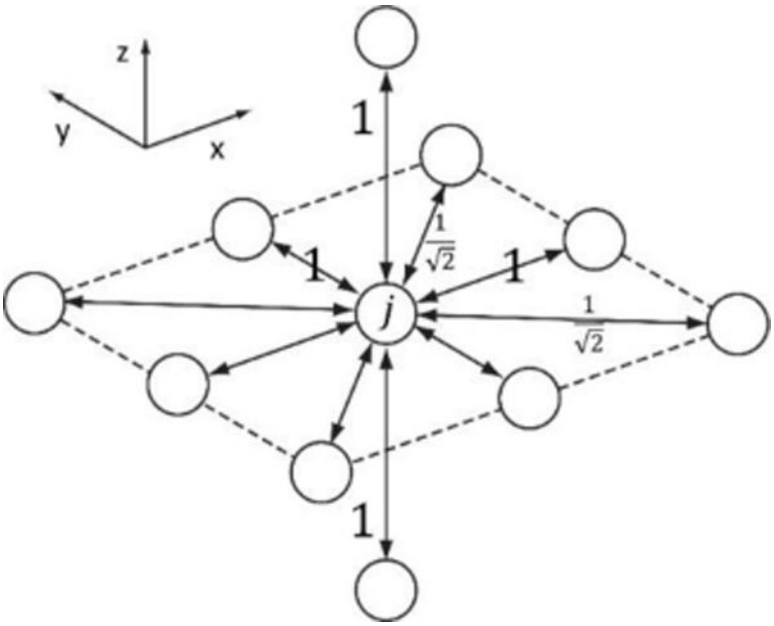

Fig.1.

Illustration of the in-plane second order neighborhood over which the penalty is effective. Conventional penalty weighting scheme with $\xi_{jk} = 1$ for horizontal and vertical pairwise neighbors, and $\frac{1}{\sqrt{2}}$ for diagonal pairwise neighbors; r_{jk} is 1 for all directions (not shown).

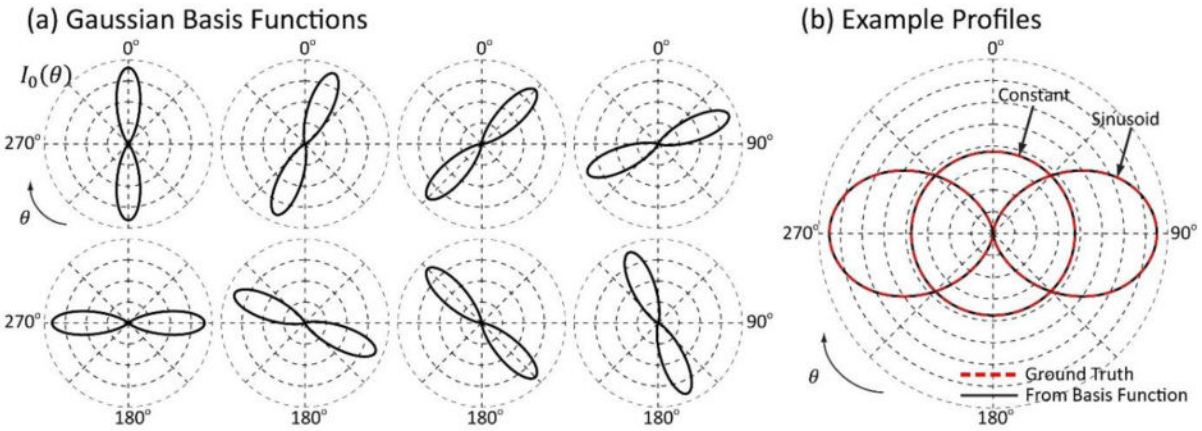

Fig.2.

(a) Polar plots of the Gaussian basis functions used for tube current modulation. The radial axis represents mAs per frame. Views 180^o apart are assigned the same weights in our investigations of a 360° circular scan. (b) A constant and a sinusoidal tube current modulation profiles represented by the Gaussian basis functions (solid) almost completely overlaps with ground truth (dashed).

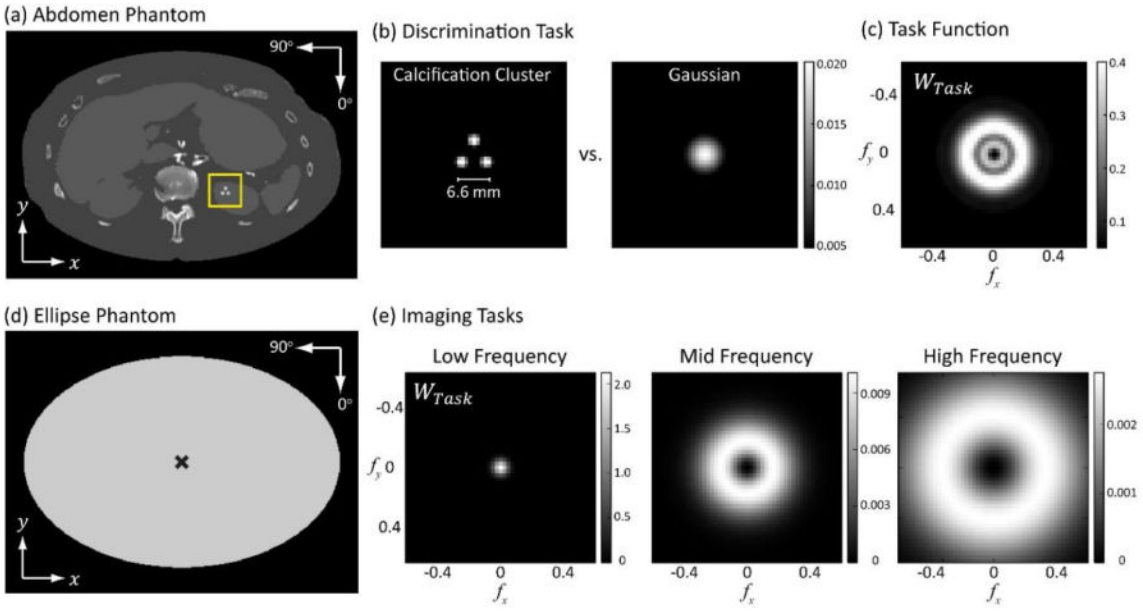

Fig. 3.

(a) The abdomen phantom with the stimulus inserted in the right kidney. (b) Discrimination task of a calcification cluster from a monolithic Gaussian. (c) The frequency domain task function of the imaging task illustrated in (b). (a), (b), and (c) are used for the six imaging strategies described in Sec.2.1. (d) A homogeneous ellipse phantom with a location of interest at the center. (e) Three task functions constructed directly in the Fourier domain presenting low, mid, and high-frequency content. (d) and (e) are used to investigate of the effect of β on the optimal tube current modulation.

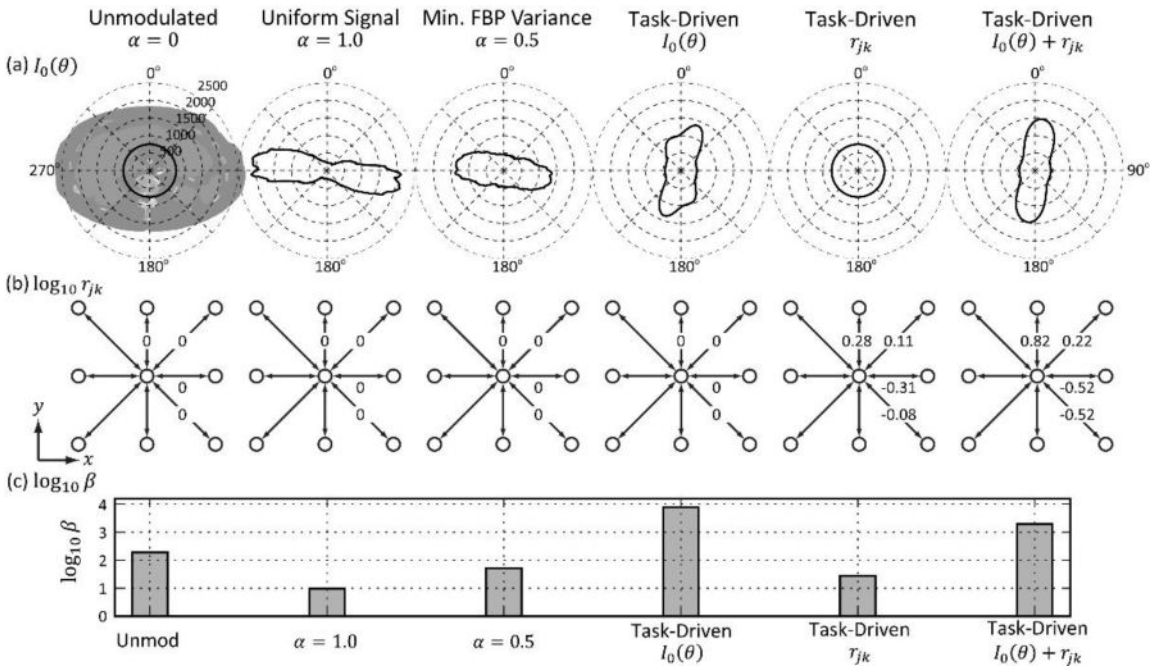

Fig.4.

The (a) tube current modulation, (b) directional penalty weights, and (c) β for the six imaging strategies detailed in Sec.B.1.6.

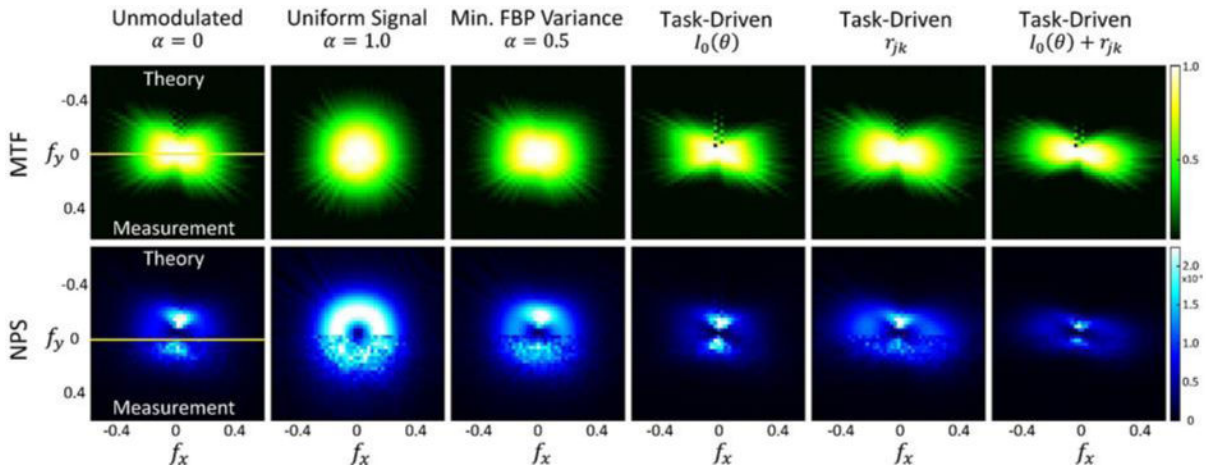

Fig.5.

The local MTF (row 1) and NPS (row 2) around the location of the imaging task for the six imaging strategies. Theoretical predictions presented at the top half of each figure are compared with empirical estimations presented at the bottom half.

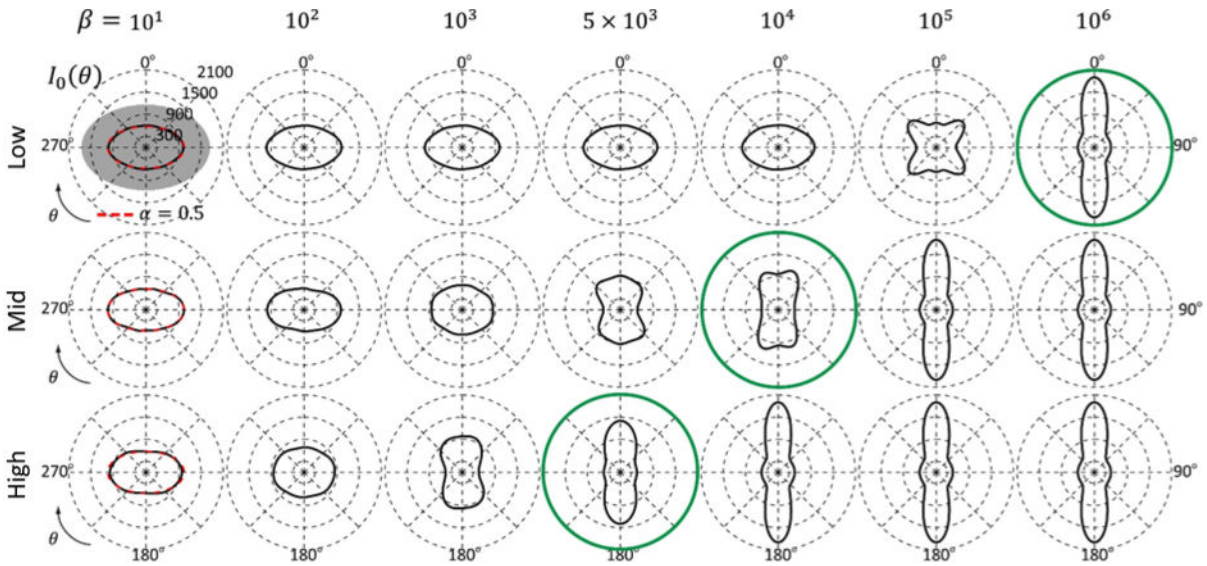

Fig.6.

Optimal tube current modulation as a function of β for three imaging tasks presenting low-, mid-, and high-frequency components. For comparison, the α = 0.5 modulation pattern is plotted as red dotted lines in the first column. The β value that yields the highest d' for each task is indicated by a green circle.

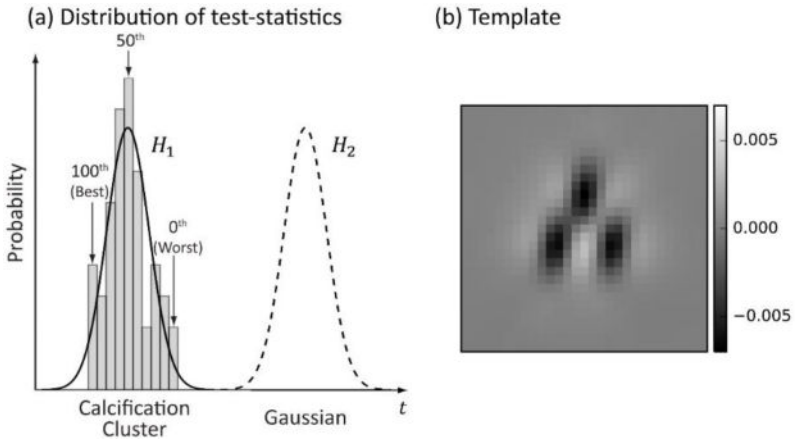

Fig. 7.

(a) Test statistics distribution for the two hypotheses under the Task-Driven $I_0(\theta) + r_{jk}$ strategy. Values for the calcification cluster hypothesis were calculated from the 50 reconstructions following Eq.(19) and are shown as the bar plot. A Gaussian fit is superimposed as the solid curve. Distribution for the monolithic Gaussian signal is approximated for purposes of illustration. (b) Template for the Task-Driven $I_0(\theta) + r_{jk}$ strategy.

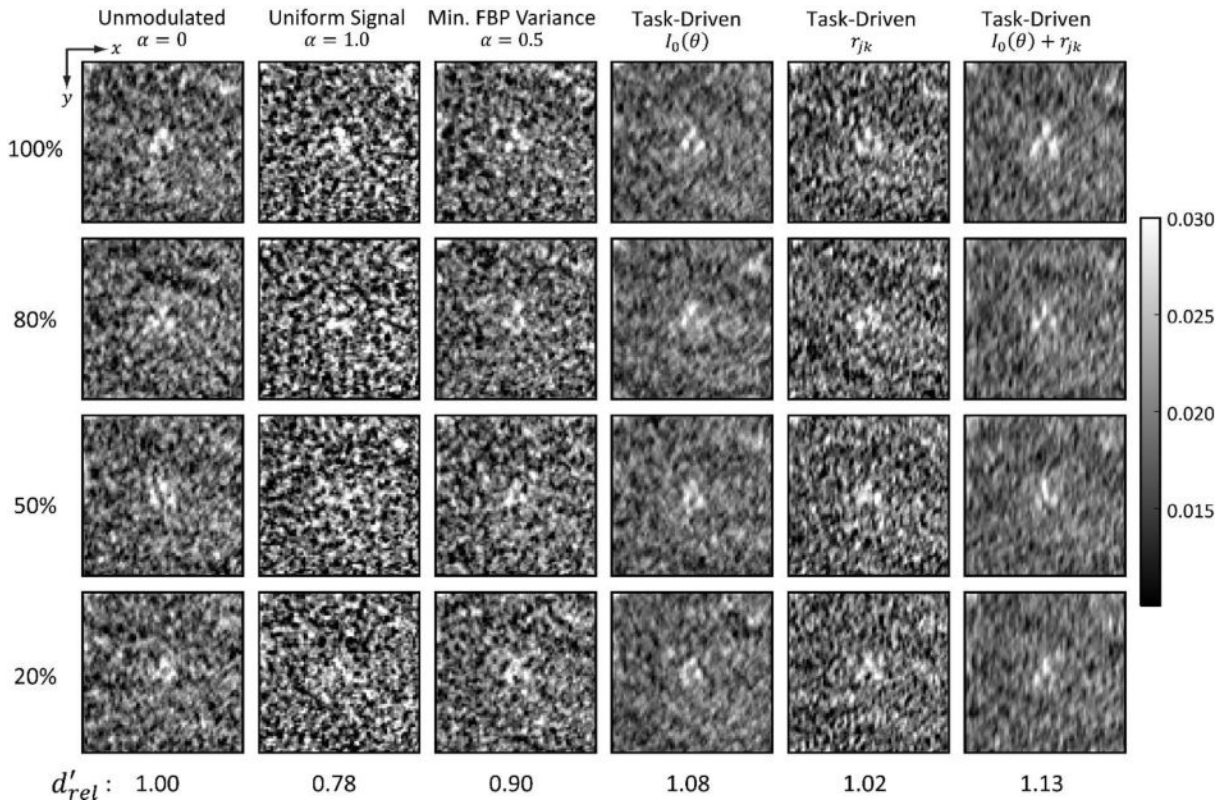

Fig.8.

Reconstruction ROIs corresponding to the 100th, 80th, 50th, and 20th percentile from the respective test statistics distrubtion for each of the six imaging strategies. Relative d' to the "Unmod" strategy are shown at the bottom.